

Excitation of unidirectional exchange spin waves by a nanoscale magnetic grating

Jilei Chen,^{1,*} Tao Yu,^{2,*} Chuanpu Liu,^{1,*} Tao Liu,^{3,*} Marco Madami,^{4,*} Ka Shen,^{5,*} Jianyu Zhang,¹ Sa Tu,¹ Md Shah Alam,¹ Ke Xia,⁶ Mingzhong Wu,³ Gianluca Gubbiotti,⁷ Yaroslav M. Blanter,² Gerrit E. W. Bauer,^{2,8,9,†} and Haiming Yu^{1,‡}

¹Fert Beijing Institute, BDBC, School of Microelectronics, Beihang University, Beijing 100191, China

²Kavli Institute of Nanoscience, Delft University of Technology, 2628 CJ Delft, The Netherlands

³Department of Physics, Colorado State University, Fort Collins, Colorado 80523, USA

⁴Dipartimento di Fisica e Geologia, Università di Perugia, Via A. Pascoli, I-06123 Perugia, Italy

⁵Department of Physics, Beijing Normal University, Beijing 100875, China

⁶Institute for Quantum Science and Engineering, Southern University of Science and Technology, Shenzhen 518055, China

⁷Istituto Officina dei Materiali del Consiglio Nazionale delle Ricerche (IOM-CNR), Sede di Perugia, c/o Dipartimento di Fisica e Geologia, Via A. Pascoli, I-06123 Perugia, Italy

⁸Institute for Materials Research, WPI-AIMR and CSNR, Tohoku University, Sendai 980-8577, Japan

⁹Zernike Institute for Advanced Materials, University of Groningen, Nijenborgh 4, 9747 AG Groningen, The Netherlands



(Received 11 March 2019; revised manuscript received 18 June 2019; published 20 September 2019)

Magnon spintronics is a prosperous field that promises beyond-CMOS technology based on elementary excitations of the magnetic order that act as information carriers for future computational architectures. Unidirectional propagation of spin waves is key to the realization of magnonic logic devices. However, previous efforts to enhance the magnetostatic surface spin wave nonreciprocity did not realize (let alone control) purely unidirectional propagation. Here we experimentally demonstrate excitation of unidirectional exchange spin waves by a nanoscale magnetic grating consisting of Co nanowires fabricated on an ultrathin yttrium iron garnet film. We explain and model the nearly perfect unidirectional excitation by the chirality of the magneto-dipolar interactions between the Kittel mode of the nanowires and the exchange spin waves of the film. Reversal of the magnetic configurations of film and nanowire array from parallel to antiparallel changes the direction of the excited spin waves. Our results raise the prospect of a chiral magnonic logic without the need to involve fragile surface states.

DOI: [10.1103/PhysRevB.100.104427](https://doi.org/10.1103/PhysRevB.100.104427)

I. INTRODUCTION

Spin waves (SWs) [1–6] can transport information in high-quality magnetic insulators such as yttrium iron garnet (YIG) [7–10] free of charge flow and with very low power dissipation. Based on the interference and nonlinear interactions, the phase information of SWs [11–15] allows the design of wave-based logic circuits [16–19] for information transmission and processing with a small environmental footprint. Surface SWs [20] are chiral, i.e., they propagate only in the direction of the outer product of the magnetization direction and surface normal and, therefore, in opposite directions on the upper and lower film surfaces/interfaces. These Damon-Eshbach (DE) modes [20] are beneficial for magnonic logic devices [21] but exist only in thick magnetic films with sizable group velocities. However, dipolar DE spin waves have small group velocities and are susceptible to surface roughness scattering [22]. Previous efforts have focused on realizing spin wave-based transport on magnetic metallic systems [23–31] with relatively high dissipation. Short-wavelength spin waves [32–39] with dispersion governed by the exchange interactions travel much faster at higher frequencies [Fig. 1(d)].

However, pure exchange spin waves are not chiral, i.e., they travel equally well in all directions. In a pioneering work Au *et al.* [40] predicted with numerical simulations that unidirectional exchange spin waves can be excited using a nanoscale magnonic transducer. Recently, Wintz *et al.* [32] observed spin waves in an intermediate regime with relatively short wavelength $\lambda = 125$ nm in small (4 μ m) permalloy thin film structures that are “nonreciprocal,” i.e., they propagate with different velocities in opposite directions.

Here we report unidirectional propagation of exchange spin waves (ESWs) down to wavelengths of 60 nm in ultrathin YIG films capped by an array of Co nanowires functioning as a nanoscale magnetic grating. The SW propagation direction can be controlled by changing the relative directions of the Co and YIG magnetizations from parallel (P state) to antiparallel (AP state). The chirality is strongly suppressed when the magnetizations are noncollinear. This property is important to realize either planar [33] or layered [34] reconfigurable magnonic crystals whose dynamic response can be controlled on demand by changing the magnetic configuration. Our observations cannot be explained by the excitation of the upper DE surface mode, because in ultrathin films ($t < 100$ nm) the mode loses its surface character and acquires a quasi-uniform profile through the film thickness: the magnetization amplitudes of the fundamental SWs that propagate in both directions normal to the (in-plane) magnetization are practically identical [41]. Instead, we find that the interlayer

*These authors contributed equally to this work.

†g.e.w.bauer@imr.tohoku.ac.jp

‡haiming.yu@buaa.edu.cn

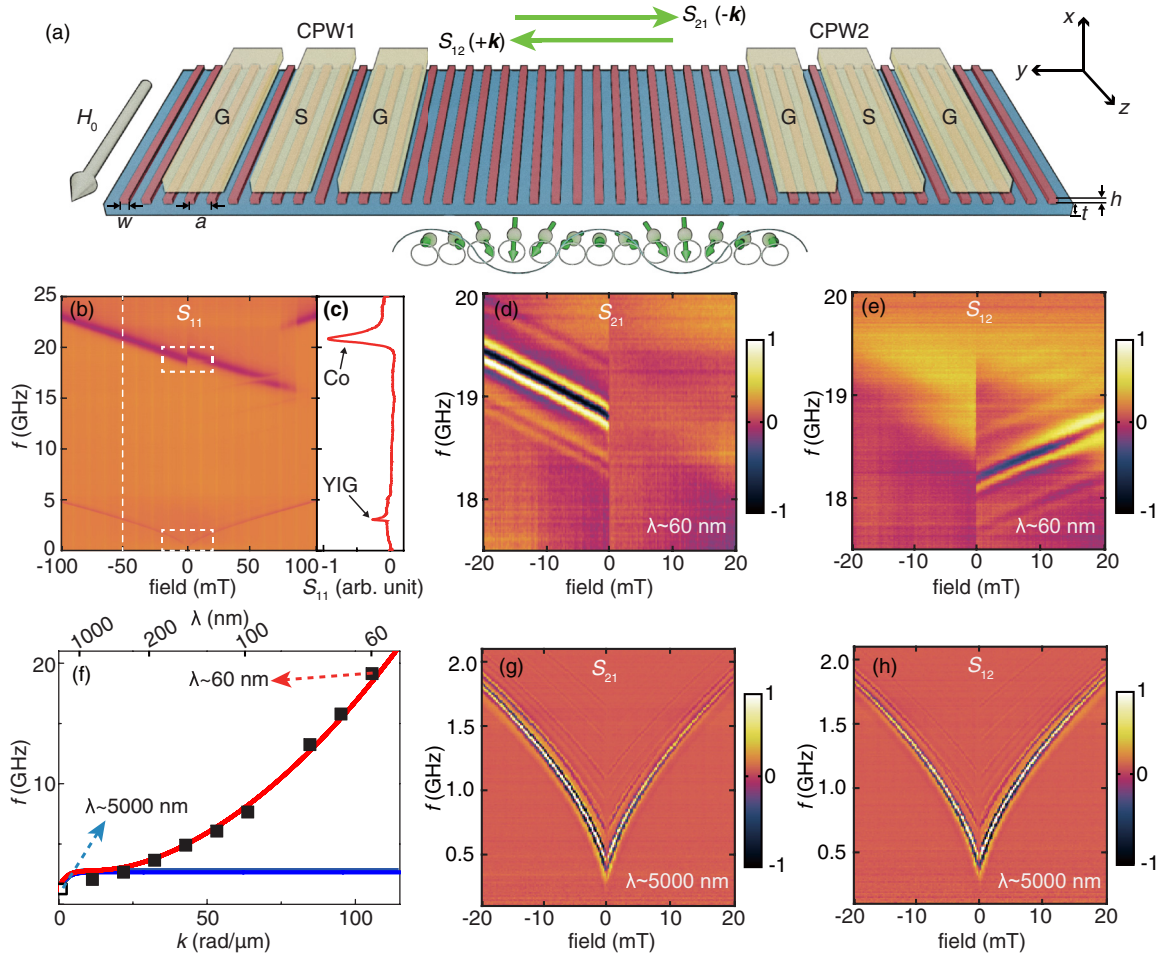


FIG. 1. Unidirectional propagation of short-wavelength exchange spin waves in Co/YIG magnetic nanostructures. (a) Sketches of propagating spin waves in YIG thin film with a Co nanowire array on top. The YIG film is magnetically much softer than the Co nanowires. We consider here the P and AP configurations controlled by an external field H_0 applied in-plane and parallel to the nanowire length (easy magnetization direction). The SWs are excited by one CPW, propagate normal to the wires, and are detected by the other CPW. The period of the nanowire array is $a = 600$ nm, and the width of a single nanowire is $w = 110$ nm. The high-frequency microwave transmission between the two waveguides mediated by SWs turns out to be unidirectional, i.e., when magnetizations are in P configuration ($H < 0$), S_{21} is finite but $S_{12} = 0$. (b) Microwave reflection spectra S_{11} measured from -100 mT to 100 mT. A line plot is extracted from the white dashed line at -50 mT and shown in panel (c). White dashed-line squares indicate the regions of exchange and dipolar SWs enlarged in panels (d) and (e) and (g) and (h), respectively. (d) The microwave transmission spectra S_{21} , carried by $-k$ SWs with wave length λ from the left to the right at negative magnetic fields, but not positive ones. (e) In contrast to panel (d) microwave transmission spectra S_{12} carried by $+k$ SWs in the opposite direction are transmitted only for positive fields. (f) SW dispersion relation. The red curve represents the exchange-dipolar SW dispersion equation (1). The blue curve gives the dispersion of pure dipolar SWs (DE modes). Black squares are data points extracted from the experiments (Supplemental Material, Fig. S8 [43]). The highest mode number $n = 20$ corresponds to a propagating ESW with wavelength $\lambda \sim 60$ nm, while the lowest-frequency modes are dipolar SWs with wavelength $\lambda \sim 5000$ nm. The low-frequency transmission spectra S_{21} (g) and S_{12} (h) are carried by (dipolar) spin waves degenerate with the YIG film Kittel mode resonance.

dynamic dipolar coupling between the nanowires and the film is responsible for the observed effect. Our theoretical model suggests a nearly perfect unidirectional excitation of SWs when magnetizations are collinear and describes the angle dependence of the microwave spectra well. In addition, the unidirectional propagation of spin waves is further confirmed by micro-Brillouin light scattering (μ -BLS) spectroscopy.

II. EXPERIMENTS

The sample and measurement setup are sketched in Fig. 1(a). We fabricated a periodic array of cobalt nanowires

directly on top of an ultrathin YIG film grown on a GGG substrate by magnetron sputtering [42,43] with period $a = 600$ nm and nanowire width $w = 110$ nm. The thickness of the YIG film is $t = 20$ nm and the Co nanowires $h = 30$ nm. The coplanar waveguides (CPWs) on top of the nanostructures excite and detect the magnetization dynamics [43]. The reflection spectrum S_{11} measured at CPW1 [Fig. 1(b)] is almost identical to S_{11} measured at CPW2 (see Supplemental Material, Fig. S1 [43]). We first saturate the magnetization of YIG and Co nanowires with a large magnetic field of -200 mT along the nanowires and then sweep the field from negative to positive values. Figure 1(c) shows a line plot

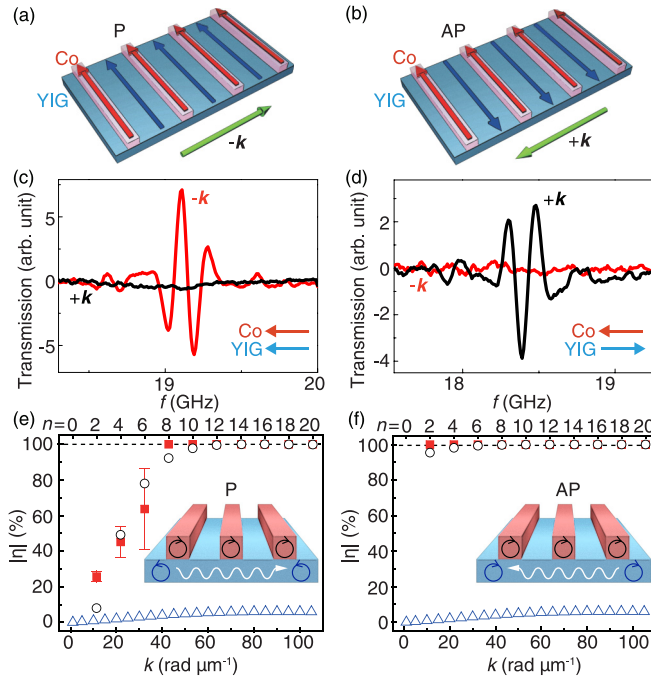


FIG. 2. Tunable chiral spin-wave excitations. Co nanowires on top of a YIG films in the P (a) and AP (b) configurations. Microwave transmission by SWs is unidirectional and chiral, i.e., only $-k$ ($+k$) SWs can be excited in the P (AP) state, and is illustrated by plotting $S_{21}^{(-k)}$ (red) and $S_{12}^{(+k)}$ (black) of the $n = 20$ ESW mode at -10 mT for the P (c) and AP state (d). We plot the degree of magnon chirality η , Eq. (2), as a function of the wave vector k for the P (e) and AP (f) configurations. The red filled squares represent the observations that agree well with micromagnetic theory (black open circles). The calculated DE nonreciprocity for dipole-exchange spin waves in the bare YIG film is very small as expected.

extracted for -50 mT. The low- (high-) frequency mode is the ferromagnetic resonance (FMR) of the YIG film (Co nanowires), respectively. The soft magnetization of the YIG film switches at a very low field, while the Co nanowires have a much larger coercivity (~ 80 mT) due to their shape anisotropy [15,44]. Therefore, the Co/YIG bilayer assumes a stable antiparallel (AP) magnetic configuration from 0 to $+80$ mT as shown in Fig. 2(b). We measured the delayed microwave propagation in both directions using a vector network analyzer (VNA) [11,12,14] over a distance of typically $15 \mu\text{m}$. We plot the transmission spectra S_{12} ($+k$ direction) and S_{21} ($-k$ direction) in Figs. 1(d) and 1(e) for applied fields from -20 mT to 20 mT in the DE configuration, i.e., parallel to the nanowires. For negative (positive) applied fields, we observe signal transmission by spin waves in the \hat{y} ($+\hat{y}$) direction only, respectively.

At FMR frequencies around 1 GHz [low-frequency mode in Fig. 1(b)] the CPWs excite long-wavelength dipolar spin waves (DSWs) in YIG and show strong transmission signals in both S_{12} ($+k$) and S_{21} ($-k$), with weak DE-mode-induced nonreciprocity [20,41]. The periodic potential generated by the Co nanowire array in principle allows the excitation of higher spin-wave modes by a homogeneous microwave field, but our observation of short-wavelength modes in YIG at frequencies up to 19 GHz is unexpected. They become visible

in the microwave transmission when nearly degenerate with the FMR of the Co nanowires for the following reason. The microwaves emitted by a CPW force the magnetization of the nanowires to precess in-phase. The latter generates a lattice-periodic dipolar field on the YIG magnetization with wave vectors $k = n\pi/a$ where a is the nanowire period and $n = 2, 4, 6, \dots$ [35]. The perpendicular standing spin waves (PSSWs) [36,37] in films have mode numbers $m = 1, 2, 3, \dots$, but they are in the present thin film upshifted to above 35 GHz and can be disregarded. For large n values, the SWs in the film are safely in the exchange-dominated regime with quadratic dispersion as shown in Fig. 1(f). More precisely, these ESWs obey the dispersion relation [45] (see Supplemental Material, Fig. S2 for an alternative derivation [43])

$$f = \mu_0 \frac{|\gamma|}{2\pi} \left[\left(H_0 + \frac{2A}{\mu_0 M_S} k^2 \right) \left(H_0 + \frac{2A}{\mu_0 M_S} k^2 + M_S \right) + M_S^2 \left(1 - \frac{1 - e^{-kt}}{kt} \right) \left(\frac{1 - e^{-kt}}{kt} \right)^{\frac{1}{2}} \right]^{\frac{1}{2}}, \quad (1)$$

where γ is the gyromagnetic ratio, H_0 is the applied field, $A = 3 \times 10^{-12}$ J/m is the exchange stiffness constant, and $\mu_0 M_S = 143.9$ kA/m is the saturation magnetization of sputtered YIG films [42]. The thickness of the YIG film $t = 20$ nm and k is the (modulus of the) wave vector normal to the magnetization. We observe multiple of these ESW modes, which allows us to map the dispersion relation equation (1) in Fig. 1(f) (see Supplemental Material, Fig. S7 for more data and Fig. S8 for the excitation efficiencies of these modes [43]). The transmission spectra [Figs. 1(d) and 1(e)] show clear interference fringes, where the group velocities $v_g = 2.7$ km/s can be extracted from the peak-to-peak frequency span Δf using $v_g = \partial\omega/\partial k = 2\pi\Delta f/(2\pi/s) = \Delta f \cdot s$ [11,12], where s is the spin-wave propagation distance being $15 \mu\text{m}$. Taking into account the damping parameter $\alpha = 8 \times 10^{-5}$ [9], a decay length of 0.3 mm can be estimated taking $l_d = v_g/2\pi\alpha f$. The microwave transmission spectra indicate a strong unidirectionality of the SW propagation, which can be controlled by a magnetic field. It changes sharply when the YIG magnetization switches from the parallel (P) to antiparallel (AP) configurations as shown in Figs. 2(a) and 2(b) with symmetry $S_{12}(\mathbf{M}) = S_{21}(-\mathbf{M})$. This phenomenology coincides with that of chiral DE surface modes on thick magnetic slabs. However, here we can exclude this explanation: First, since the YIG film is so thin, there are no surface modes even in the dipolar regime at low frequencies, because the amplitudes of left- and right-moving spin waves are practically identical [Figs. 1(g) and 1(h)]. Moreover, the short-wavelength modes are in the exchange regime at frequencies much higher than DE limitations [open blue triangles in Fig. 1(f)]. We therefore conclude that the magnetic nanowires generate a unidirectionality that does not exist in the bare film (see Supplemental Material, Fig. S9 for more the calculation of nonreciprocity effect for dipole-exchange spin waves without nanoscale gratings [43]). Summarizing our observations, the Co/YIG bilayer in the P (AP) configuration allows SW propagation only in the $-k$ ($+k$) direction and appear to be chiral. We can quantify

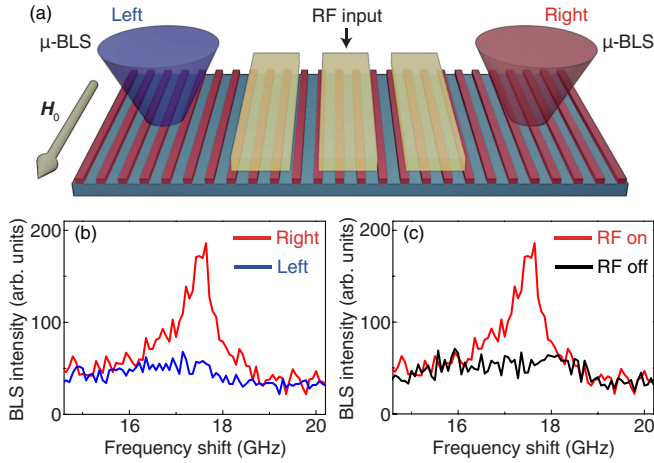


FIG. 3. (a) Schematic drawing of the μ -BLS geometry on a Co nanowire array on YIG with parameters [defined in Fig. 1(a)] $w = 400$ nm, $a = 600$ nm, and $h = 30$ nm. The applied external field ($H = 20$ mT) generates the P state, and the position of laser spots is indicated. (b) Comparison between two μ -BLS spectra measured as a function of RF frequency on the right (red) and left (blue) sides of the antenna, respectively. (c) Comparison between two μ -BLS spectra measured on the same (right) side of the antenna with and without RF pumping.

the magnon chirality in terms of the ratio

$$\eta = \frac{S_{21}^{(-k)} - S_{12}^{(+k)}}{S_{21}^{(-k)} + S_{12}^{(+k)}}, \quad (2)$$

where $|\eta| = 1$ indicates perfect unidirectional spin-wave propagation. $|\eta|$ increases with the increasing mode number n as shown in Figs. 2(e) and 2(f) for P and AP states, respectively. The unidirectionality appears to be more easily formed in the antiparallel configuration, which may be an outcome of the fact that spin precession always favors the “anticlockwise” precession around the external field. The exchange spin waves with $n \geq 8$ [cf. Fig. 1(d)] are fully chiral. The open blue triangles in Figs. 2(e) and 2(f) are the calculated nonreciprocity factors Eq. (5) based on the model from Ref. [45] (See Supplemental Materials, Fig. S9 for details [43]). The observed unidirectionality therefore cannot be accounted for by a DE nonreciprocity extended into the exchange regime.

We confirmed the unidirectionality of SW propagation by microfocused Brillouin light scattering (μ -BLS), which allows us to map the SW intensity with a lateral resolution of about 250 nm where spin waves are excited [46]. A single CPW antenna excites SWs in the specially designed sample sketched in Fig. 3(a). Figure 3(b) shows the μ -BLS spectra measured on both sides of the antenna under the same experimental conditions (P state, $H = 20$ mT) as a function of the RF pumping signal. A spin signal is detected only on the right side of the antenna. By comparing μ -BLS signals on the same (right) side for RF generator ON and OFF, we confirm that the thermal spin signal background is at resonance much smaller than the excited spin signal [Fig. 3(c)]. With a reversed applied field (not shown) the signal is observed only on the left side.

III. MODELING

We now turn to an explanation of the observed high magnon chirality of nominally nonchiral exchange spin waves. As discussed above, either the interface exchange or the dipolar interaction between the Co nanowires and YIG thin film is responsible for the effect. Since the former cannot generate the observed chirality, we focus here on the latter. Assuming perfect lattice and translational periodicity in the film plane and disregarding high-frequency PSSWs, the micromagnetic problem becomes one-dimensional, with interaction Hamiltonian in second quantization

$$\hat{H}/\hbar = \sum_n (g_n^+ \hat{\beta}_{+k} \hat{\alpha}^\dagger + g_n^- \hat{\beta}_{-k} \hat{\alpha}^\dagger), \quad (3)$$

where $\hat{\alpha}^\dagger$ denotes the magnon creation operator for the Kittel mode of the Co nanowires, $\hat{\beta}_{+k}$ and $\hat{\beta}_{-k}$ are the magnon annihilation operators for the $+\mathbf{k}$ and $-\mathbf{k}$ spin waves of the YIG film, respectively, and

$$g_n^+ = -\gamma \sigma_n \sqrt{(\mu_0 M_S^{\text{Co}})(\mu_0 M_S^{\text{YIG}})} \int \hat{\mathbf{m}}_{\text{Co}}^* \tilde{\Lambda}^* \hat{\mathbf{m}}_{\text{YIG}} e^{kx} dx, \\ g_n^- = -\gamma \sigma_n \sqrt{(\mu_0 M_S^{\text{Co}})(\mu_0 M_S^{\text{YIG}})} \int \hat{\mathbf{m}}_{\text{Co}}^* \tilde{\Lambda} \hat{\mathbf{m}}_{\text{YIG}} e^{kx} dx, \quad (4)$$

is the coupling strength for spin waves with wave numbers $k = n\pi/a$ with $n = 2, 4, 6, \dots$ propagating along the $+\hat{y}$ direction for g_n^+ and $-\hat{y}$ direction for g_n^- . Here M_S^{Co} and M_S^{YIG} are the saturation magnetization of Co and YIG. In the P state, both magnetization are along the $-\hat{z}$ direction and the form factor $\sigma_n = \frac{2}{n\pi} \sin(\frac{kn}{2})(1 - e^{-kh})$. $\hat{\mathbf{m}}_{\text{Co}} = (\hat{m}_x, \hat{m}_y)$ is the Co magnetization precession of the nanowire Kittel mode,

where $\hat{m}_x = (\frac{a}{4\hbar w} \sqrt{\frac{H_0 + M_S^{\text{Co}} N_{yy}}{H_0 + M_S^{\text{Co}} N_{xx}}})^{\frac{1}{2}}$ and $\hat{m}_y = (\frac{a}{4\hbar w} \sqrt{\frac{H_0 + M_S^{\text{Co}} N_{xx}}{H_0 + M_S^{\text{Co}} N_{yy}}})^{\frac{1}{2}}$, while N_{xx} and N_{yy} are the demagnetization factors [15,44] of a long wire. $\tilde{\Lambda} = (\begin{smallmatrix} 1 & i \\ i & -1 \end{smallmatrix})$ and $\hat{\mathbf{m}}_{\text{YIG}} = (\hat{m}_x^k, \hat{m}_y^k)$ describes the YIG magnetization precession of the SW modes. In the exchange regime, the spin precession is circular with $i\hat{m}_x^k = \hat{m}_y^k = i(\frac{1}{4t})^{\frac{1}{2}}$. Derivations are given in the Supplemental Material [43] (see, also, Refs. [15,27,47–64]) and Ref. [65].

$|g_n^+| \neq |g_n^-|$ implies that the interlayer dynamic dipolar coupling between magnons in Co nanowires and YIG thin film is indeed chiral. We find for the magnon chirality factor equation (2)

$$\eta = \frac{(g_n^-/g_n^+)^2 - 1}{(g_n^-/g_n^+)^2 + 1}. \quad (5)$$

In the P configuration and the exchange regime $g_n^- \neq 0$ and $g_n^+ = 0$, indicating perfect chirality or $\eta = 1$. For AP magnetizations, $\hat{\mathbf{m}}_{\text{YIG}} = (\hat{m}_x^k, -\hat{m}_y^k)$ yields $g_n^- = 0$ and $g_n^+ \neq 0$, indicating a reversed chirality compared with the P state as observed in perfect agreement with the analysis of the experimental data shown in Figs. 2(e) and 2(f). The modeling results in Figs. 2(e) and 2(f) agree with experimental findings also for longer wavelength modes with partial chirality.

IV. ANGULAR DEPENDENCE

We can force the magnetizations of the Co nanowires and the YIG thin film to form a finite angle θ by relatively

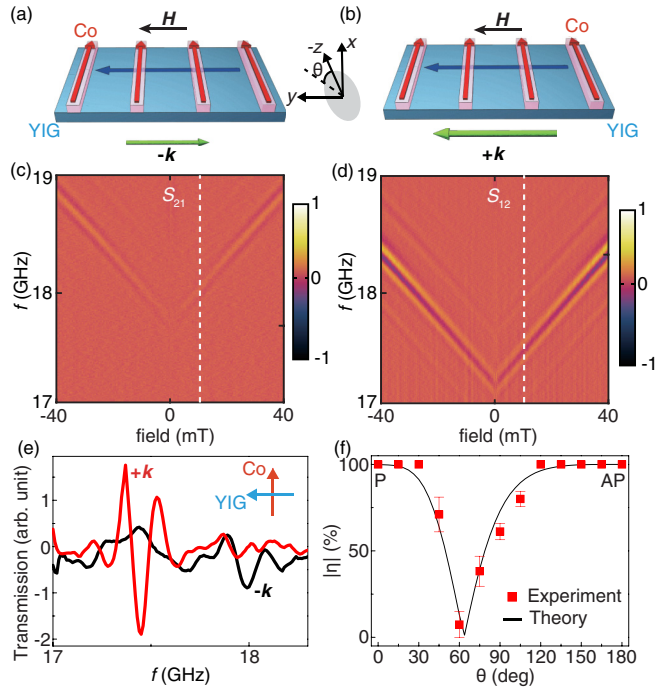


FIG. 4. Spin wave propagation in noncollinear configurations. Microwave transmission by SWs with wave vector $-k$ (a) and $+k$ (b) when the film magnetization (blue arrow) is normal to the nanowires with magnetization indicated by the red arrows with (in-plane) angle $\theta = 90^\circ$ (see inset). The SW transmission spectra S_{21} for $-k$ SWs (c) and S_{12} for $+k$ SWs (d) as function of an applied field H along the y axis after saturating the nanowire magnetization with a -200 mT field along z . (e) Transmission spectra for $\theta = 90^\circ$ at 10 mT for S_{21} ($-k$, black) and S_{12} ($+k$, red) for $n = 20$ as indicated by the white dashed lines in panels (c) and (d). The inset illustrates the magnetization directions. (f) θ dependence of the magnon chirality η as observed (red squares) and calculated (black line). $\theta = 0^\circ$ and 180° indicate the P and AP states, respectively.

weak external magnetic fields [see Figs. 4(a) and 4(b) for $\theta = 90^\circ$] because the YIG coercivity is very small [42]. The transmission spectra were recorded after saturating the nanowire magnetizations with an applied field of -200 mT in the \hat{z} direction. The magnetization of the YIG thin film is saturated already at a relatively small fields (< 50 mT) along \hat{y} but does not affect the magnetization of the Co nanowires along the \hat{z} axis due to their large demagnetization field (~ 80 mT). We observe in Figs. 4(c) and 4(d) that at $\theta = 90^\circ$ the chirality is broken, i.e., SWs propagate in both $+k$ and $-k$ directions. A finite nonreciprocity persists in the spectra at a field of 10 mT in Fig. 4(e), different from a DE-mode-induced nonreciprocity that would have been transformed into fully reciprocal backward-moving volume modes. We show the magnon chirality $|\eta|$ of the $n = 20$ ESW extracted from the experiments as a function of θ in Fig. 4(f). The micromagnetic model equations (4) and (5) (solid black curve) reproduce the observed angular dependence of the chirality (red squares) very well (see Supplemental Material, Fig. S3 for details [43]). The frequency shift $\delta f \sim 0.5$ GHz between $+k$ and $-k$ spin waves in Fig. 4(e) is a feature beyond the interlayer dipolar coupling model. The chirality persists

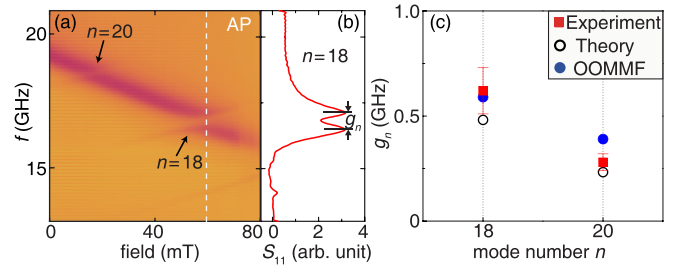


FIG. 5. Total coupling strength characterized by the anticrossing gaps. (a) SW reflection spectra S_{11} measured in the AP state. Arrows indicate two observed anticrossings for $n = 18$ and $n = 20$ ESWs, respectively. (b) A single SW spectrum measured at 60 mT which allows extraction of the anticrossing gap g_n^+ of the $n = 18$ mode. (c) Anticrossing gaps for two SW modes: Red squares are experimental data; black circles are derived from the theoretical model; blue dots are the results of micromagnetic simulations with the OOMMF code [69].

in another sample with an Al_2O_3 spacer between Co and YIG (Supplemental Material, Fig. S4 [43]) indicating that the interlayer dynamic dipolar coupling is the key mechanism for the observed chirality. On the other hand, the insulating barrier quenches the frequency shift with θ , which we therefore associate with the Co-YIG exchange coupling [35,37,66] and an associated exchange-spring magnetization texture or an interfacial Dzyaloshinskii-Moriya interaction [67].

V. COUPLING STRENGTH

The interaction between the magnetic modes in the nanowire array and the continuous film is strong; i.e., total coupling strength $g_n = |g_n^-| + |g_n^+|$ can be measured in terms of the anticrossing gap between the Kittel mode of Co nanowires and the YIG SW modes [35,37,66].

Figure 5(a) shows SW reflection spectra measured in the AP state. Two clear anticrossings indicated couplings between the Kittel mode of the Co nanowires and two ESWs in YIG. The anticrossing for the mode $n = 16$ [see Fig. 1(b) for the full spectra] is only partially resolved because the AP state switches back to the P state at fields of ~ 80 mT that overcome the demagnetizing field of the Co nanowires. The interaction splits the resonance peak at $n = 18$ of the line plot in Fig. 5(b) by $g_n \cong 0.62$ GHz. This anticrossing also occurs when a magnetic field of 60 mT is rotated in the film plane (Supplemental Material, Fig. S6 [43]). From the observed line widths, we extract a dissipation rate $\kappa_m^{\text{Co}} \cong 0.81$ GHz for the Kittel mode in Co and $\kappa_m^{\text{YIG}} \cong 0.11$ GHz for the exchange spin waves in YIG. Since $\kappa_m^{\text{YIG}} < g_n < \kappa_m^{\text{Co}}$ we are in the magnetically induced transparency but not the strong coupling regime [68]. We plot the computed purely dipolar coupling using Eq. (4) in Fig. 5(c) as open circles. Since the magnon chirality rate $|\eta| \approx 100\%$ for high-order exchange spin waves [Fig. 2(f)], $g_n^+ \approx g_n$ and $g_n^- \approx 0$ for the AP states. Micromagnetic simulations based on the object-oriented micromagnetic framework (OOMMF) [69] confirm the anticrossing features (see Supplemental Material, Fig. S5 for the details of the simulations [43]) and the computed gaps are the blue dots in Fig. 5(c).

VI. CONCLUSIONS

In conclusion, we report generation of unidirectional beams of nonchiral exchange spin waves in YIG film with wavelengths down to 60 nm when brought to resonance with a Co nanowire grating coupler [40,70,71] on top of the film. The spin-wave direction can be reversed by switching the magnetic configuration of Co nanowire array and YIG film from parallel to antiparallel. We explain and model the experimental results by the interlayer dipolar coupling between Co and YIG that can be assessed by the anticrossing gaps at the resonance. We observe and model a nearly perfect chirality for magnon propagation in a collinear magnetic configuration. Noncollinear applied magnetic fields break the symmetry and suppress chirality. Interestingly, our findings appear to be a magnonic counterpart of the unidirectional excitation of surface plasmon polariton waves by circularly polarized electric dipoles [72], but highlight remarkable differences as well. The ability to excite unidirectional and easily switchable exchange spin waves with high group velocity can become a

key functionality in reconfigurable nanomagnonic logic and computing devices [6,33,73].

ACKNOWLEDGMENTS

The authors thank K. Buchanan for helpful discussions. We wish to acknowledge the support by NSF China under Grants No. 11674020 and No. U1801661 and the 111 talent program B16001. T.Y., G.B., and Y.B. were supported by the Netherlands Organization for Scientific Research (NWO). G.B. was supported by Japan Society for the Promotion of Science Kakenhi Grants-in-Aid for Scientific Research (Grants No. 26103006 and No. 19H006450). K.X. thanks the National Key Research and Development Program of China (Grants No. 2017YFA0303304 and No. 2018YFB0407601) and the National Natural Science Foundation of China (Grants No. 61774017 and No. 11734004). K.S. was supported by the Fundamental Research Funds for the Central Universities (Grant No. 2018EYT02). T.L. and M.W. were supported by the US National Science Foundation (Grant No. EFMA-1641989).

-
- [1] A. V. Chumak, V. I. Vasyuchka, A. A. Serga, and B. Hillebrands, *Nat. Phys.* **11**, 453 (2015).
 - [2] V. V. Kruglyak, S. O. Demokritov, and D. Grundler, *J. Phys. D* **43**, 264001 (2010).
 - [3] V. E. Demidov, S. Urazhdin, G. de Loubens, O. Klein, V. Cros, A. Anane, and S. O. Demokritov, *Phys. Rep.* **673**, 1 (2017).
 - [4] H. Yu, J. Xiao, and P. Pirro, *J. Magn. Magn. Mater.* **450**, 1 (2018).
 - [5] A. Haldar, D. Kumar, and A. O. Adeyeye, *Nat. Nanotechnol.* **11**, 437 (2016).
 - [6] K. Wagner, A. Kákay, K. Schultheiss, A. Henschke, T. Sebastian, and H. Schultheiss, *Nat. Nanotechnol.* **11**, 432 (2016).
 - [7] A. A. Serga, A. V. Chumak, and B. Hillebrands, *J. Phys. D* **43**, 264002 (2010).
 - [8] Y. Kajiwara, K. Harii, S. Takahashi, J. Ohe, K. Uchida, M. Mizuguchi, H. Umezawa, H. Kawai, K. Ando, K. Takanashi, S. Maekawa, and E. Saitoh, *Nature (London)* **464**, 262 (2010).
 - [9] H. Chang, P. Li, W. Zhang, T. Liu, A. Hoffmann, L. Deng, and M. Wu, *IEEE Magn. Lett.* **5**, 6700104 (2014).
 - [10] L. J. Cornelissen, J. Liu, R. A. Duine, J. B. Youssef, and B. J. van Wees, *Nat. Phys.* **11**, 1022 (2015).
 - [11] V. Vlaminck and M. Bailleul, *Science* **322**, 410 (2008).
 - [12] S. Neusser, G. Durr, H. G. Bauer, S. Tacchi, M. Madami, G. Woltersdorf, G. Gubbiotti, C. H. Back, and D. Grundler, *Phys. Rev. Lett.* **105**, 067208 (2010).
 - [13] J. Ding, M. Kostylev, and A. O. Adeyeye, *Phys. Rev. Lett.* **107**, 047205 (2011).
 - [14] H. Yu, O. Allivy Kelly, V. Cros, R. Bernard, P. Bortolotti, A. Anane, F. Brandl, R. Huber, I. Stasinopoulos, and D. Grundler, *Sci. Rep.* **4**, 6848 (2014).
 - [15] J. Ding, M. Kostylev, and A. O. Adeyeye, *Phys. Rev. B* **84**, 054425 (2011).
 - [16] A. Khitun, M. Bao, and K. L. Wang, *J. Phys. D* **43**, 264005 (2010).
 - [17] T. Schneider, A. A. Serga, B. Leven, B. Hillebrands, R. L. Stamps, and M. P. Kostylev, *Appl. Phys. Lett.* **92**, 022505 (2008).
 - [18] J. Lan, W. Yu, R. Wu, and J. Xiao, *Phys. Rev. X* **5**, 041049 (2015).
 - [19] G. Csaba, A. Papp, and W. Porod, *Phys. Lett. A* **381**, 1471 (2017).
 - [20] R. W. Damon and J. R. Eshbach, *J. Phys. Chem. Solids* **19**, 308 (1961).
 - [21] M. Jamali, J. H. Kwon, S.-M. Seo, K.-J. Lee, and H. Yang, *Sci. Rep.* **3**, 3160 (2013).
 - [22] T. Yu, S. Sharma, Y. M. Blanter, and G. E. W. Bauer, *Phys. Rev. B* **99**, 174402 (2019).
 - [23] P. Khalili-Amiri, B. Rejaei, M. Vroubel, and Y. Zhuang, *Appl. Phys. Lett.* **91**, 062502 (2007).
 - [24] T. Schneider, A. A. Serga, T. Neumann, B. Hillebrands, and M. P. Kostylev, *Phys. Rev. B* **77**, 214411 (2008).
 - [25] V. E. Demidov, M. P. Kostylev, K. Rott, P. Krzysteczko, G. Reiss, and S. O. Demokritov, *Appl. Phys. Lett.* **95**, 112509 (2009).
 - [26] K. Sekiguchi, K. Yamada, S. M. Seo, K. J. Lee, D. Chiba, K. Kobayashi, and T. Ono, *Appl. Phys. Lett.* **97**, 022508 (2010).
 - [27] M. P. Kostylev, *J. Appl. Phys.* **113**, 053907 (2013).
 - [28] M. Mruczkiewicz, M. Krawczyk, G. Gubbiotti, S. Tacchi, Yu. A. Filimonov, and S. A. Nikitov, *New J. Phys.* **15**, 113023 (2013).
 - [29] K. Di, S. X. Feng, S. N. Piramanayagam, V. L. Zhang, H. S. Lim, S. C. Ng, and M. H. Kuok, *Sci. Rep.* **5**, 10153 (2015).
 - [30] J. H. Kwon, J. Yoon, P. Deorani, J. M. Lee, J. Sinha, K.-J. Lee, M. Hayashi, and H. Yang, *Sci. Adv.* **2**, e1501892 (2016).
 - [31] M. Mruczkiewicz, P. Graczyk, P. Lupo, A. Adeyeye, G. Gubbiotti, and M. Krawczyk, *Phys. Rev. B* **96**, 104411 (2017).
 - [32] S. Wintz, V. Tiberkevich, M. Weigand, J. Raabe, J. Lindner, A. Erbe, A. Slavin, and J. Fassbender, *Nat. Nanotechnol.* **11**, 948 (2016).
 - [33] D. Grundler, *Nat. Phys.* **11**, 438 (2015).

- [34] G. Gubbiotti, X. Zhou, Z. Haghshenasfard, M. G. Cottam, and A. O. Adeyeye, *Phys. Rev. B* **97**, 134428 (2018).
- [35] J. Chen, C. Liu, T. Liu, Y. Xiao, K. Xia, G. E. W. Bauer, M. Wu, and H. Yu, *Phys. Rev. Lett.* **120**, 217202 (2018).
- [36] C. Kittel, *Phys. Rev.* **110**, 1295 (1958).
- [37] H. Qin, S. J. Hämäläinen, and S. van Dijken, *Sci. Rep.* **8**, 5755 (2018).
- [38] C. Liu, J. Chen, T. Liu, F. Heimbach, H. Yu, Y. Xiao, J. Hu, J. Hu, M. Liu, H. Chang, T. Stueckler, Y.-G. Zhang, Y. Zhang, P. Gao, Z. Liao, D. Yu, K. Xia, L. Na, W. Zhao, and M. Wu, *Nat. Commun.* **9**, 738 (2018).
- [39] S. J. Hämäläinen, F. Brandl, K. J. A. Franke, D. Grundler, and S. van Dijken, *Phys. Rev. Appl.* **8**, 014020 (2017).
- [40] Y. Au, E. Ahmad, O. Dmytriiev, M. Dvornik, T. Davison, and V. V. Kruglyak, *Appl. Phys. Lett.* **100**, 182404 (2012).
- [41] K. L. Wong, L. Bi, M. Bao, Q. Wen, J. P. Chatelon, Y.-T. Lin, C. A. Ross, H. Zhang, and K. L. Wang, *Appl. Phys. Lett.* **105**, 232403 (2014).
- [42] T. Liu, H. Chang, V. Vlaminck, Y. Sun, M. Kabatek, A. Hoffmann, L. Deng, and M. Wu, *J. Appl. Phys.* **115**, 87 (2014).
- [43] See Supplemental Material at <http://link.aps.org/supplemental/10.1103/PhysRevB.100.104427> for S_{22} spectra, details of the theoretical model, angle-dependent spectroscopy, control measurements with a spacer, details of the micromagnetic simulations, transmission spectra of some other ESW modes, spin wave resonance frequency extraction, and the measurement techniques.
- [44] J. Topp, D. Heitmann, M. P. Kostylev, and D. Grundler, *Phys. Rev. Lett.* **104**, 207205 (2010).
- [45] B. A. Kalinikos and A. N. Slavin, *J. Phys. C: Solid State Phys.* **19**, 7013 (1986).
- [46] M. Madami, G. Gubbiotti, S. Tacchi, and G. Carlotti, in *Solid State Physics*, edited by R. E. Camley and R. L. Stamps (Academic Press, Burlington, MA, 2012), Vol. 63, p. 79.
- [47] C. Kittel, *Quantum Theory of Solids* (Wiley, New York, 1963).
- [48] C. Kittel, *Phys. Rev.* **73**, 155 (1948).
- [49] R. Verba, G. Melkov, V. Tiberkevich, and A. Slavin, *Phys. Rev. B* **85**, 014427 (2012).
- [50] L. R. Walker, *Phys. Rev.* **105**, 390 (1957).
- [51] L. D. Landaul and E. M. Lifshitz, *Electrodynamics of Continuous Media*, 2nd ed. (Butterworth-Heinenann, Oxford, 1984).
- [52] B. A. Kalinikos, *Sov. J. Phys.* **24**, 718 (1981).
- [53] K. Yu. Guslienko, S. O. Demokritov, B. Hillebrands, and A. N. Slavin, *Phys. Rev. B* **66**, 132402 (2002).
- [54] V. Vlaminck and M. Bailleul, *Phys. Rev. B* **81**, 014425 (2010).
- [55] F. Zighem, Y. Roussigne, S.-M. Cherif, and P. Moch, *J. Phys.: Condens. Matter* **19**, 176220 (2007).
- [56] R. E. De Wames and T. Wolfram, *Appl. Phys. Lett.* **15**, 297 (1969).
- [57] T. Wolfram and R. E. De Wames, *Phys. Rev. Lett.* **24**, 1489 (1970).
- [58] R. L. Stamps and B. Hillebrands, *Phys. Rev. B* **44**, 12417 (1991).
- [59] R. L. Stamps, *Phys. Rev. B* **49**, 339 (1994).
- [60] M. J. Hurben and C. E. Patton, *J. Magn. Magn. Mater.* **139**, 263 (1995).
- [61] A. Kamra and W. Belzig, *Phys. Rev. Lett.* **116**, 146601 (2016).
- [62] T. Holstein and H. Primakoff, *Phys. Rev.* **58**, 1098 (1940).
- [63] B. A. Kalinikos, M. P. Kostylev, N. V. Kozhus, and A. N. Slavin, *J. Phys.: Condens. Matter* **2**, 9861 (1990).
- [64] G. T. Rado and J. R. Weertman, *J. Phys. Chem. Solids* **11**, 315 (1959).
- [65] T. Yu, C. Liu, H. Yu, Y. M. Blanter, and G. E. W. Bauer, *Phys. Rev. B* **99**, 134424 (2019).
- [66] S. Klingler, V. Amin, S. Geprägs, K. Ganzhorn, H. Maier-Flaig, M. Althammer, H. Huebl, R. Gross, R. D. McMichael, M. D. Stiles, S. T. B. Goennenwein, and M. Weiler, *Phys. Rev. Lett.* **120**, 127201 (2018).
- [67] F. Garcia-Sanchez, P. Borys, A. Vansteenkiste, J. V. Kim, and R. L. Stamps, *Phys. Rev. B* **89**, 224408 (2014).
- [68] X. Zhang, C.-L. Zou, L. Jiang, and H. X. Tang, *Phys. Rev. Lett.* **113**, 156401 (2014).
- [69] M. Donahue and D. Porter, OOMMF User's Guide, Version 1.0, National Institute of Standards and Technology, Gaithersburg, MD, interagency report NISTIR 6376 edition, <http://math.nist.gov/oommf> (Aug. 2006).
- [70] H. Yu, G. Duerr, R. Huber, M. Bahr, T. Schwarze, F. Brandl, and D. Grundler, *Nat. Commun.* **4**, 2702 (2013).
- [71] Q. Wang, P. Pirro, R. Verba, A. Slavin, B. Hillebrands, and A. V. Chumak, *Sci. Adv.* **4**, e1701517 (2018).
- [72] F. J. Rodríguez-Fortuño, G. Marino, P. Ginzburg, D. O'Connor, A. Martínez, G. A. Wurtz, and A. V. Zayats, *Science* **328**, 328 (2013).
- [73] S. J. Hämäläinen, M. Madami, H. Qin, G. Gubbiotti, and S. van Dijken, *Nat. Commun.* **9**, 4853 (2018).

Supplemental Materials for
Excitation of unidirectional exchange spin waves by a nanoscale magnetic
grating

Jilei Chen ^{1,†}, Tao Yu ^{2,†}, Chuanpu Liu ^{1,†}, Tao Liu ^{3,†}, Marco Madami ^{4,†}, Ka Shen ^{5,†}, Jianyu Zhang ¹, Sa Tu ¹, Md Shah Alam ¹, Ke Xia ⁶, Mingzhong Wu ³, Gianluca Gubbiotti ⁷, Yaroslav M. Blanter ², Gerrit E. W. Bauer ^{2,8,9,*} and Haiming Yu ^{1,*}

¹*Fert Beijing Institute, BDBC, School of Microelectronics, Beihang University, Beijing, China.*

²*Kavli Institute of Nanoscience, Delft University of Technology, Delft, The Netherlands.*

³*Department of Physics, Colorado State University, Fort Collins, Colorado, USA.*

⁴*Dipartimento di Fisica e Geologia, Università di Perugia, Perugia, Italy.*

⁵*Department of Physics, Beijing Normal University, Beijing, China.*

⁶*Institute for Quantum Science and Engineering, Southern University of Science and Technology, Shenzhen, China.*

⁷*Istituto Officina dei Materiali del Consiglio Nazionale delle Ricerche (IOM-CNR), Sede di Perugia, c/o Dipartimento di Fisica e Geologia, Via A. Pascoli, I-06123 Perugia, Italy.*

⁸*Institute for Materials Research, WPI-AIMR and CSNR, Tohoku University, Sendai, Japan.*

⁹*Zernike Institute for Advanced Materials, University of Groningen, Groningen, The Netherlands.*

† These authors contributed equally to this work.

* Corresponding authors: g.e.w.bauer@imr.tohoku.ac.jp; haiming.yu@buaa.edu.cn

1. Full range spectra of reflection signal S_{22}

Fig. S1 shows the measured microwave reflection spectrum S_{22} with applied field parallel to the Co nanowires. The lowest branch is the DE mode spin wave resonance excited by the CPW. The highest branch is the ferromagnetic resonance of the Co nanowires. The spectra show clear evidence of P (AP) configurations: when sweeping the field from -100 mT, the magnetization of the YIG film and the Co nanowires are initially parallel, but the magnetization of the magnetically soft YIG switches by weak positive fields while the magnetization of Co nanowires remains initially unchanged due to the large form anisotropy. The magnetization of Co nanowires switches at about 70 mT, recovering the P configuration in the opposite direction.

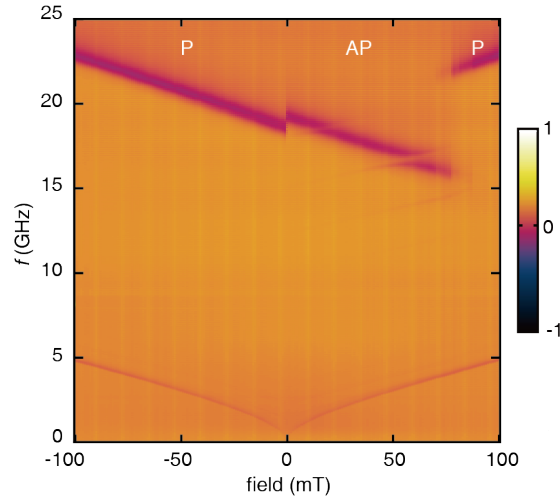


Fig. S1. Color-coded reflection spectra S_{22} . The external magnetic field first saturates the magnetizations at -200 mT and is then swept from -100 mT to 100 mT.

2. Theoretical model

We model the magnetic grating or nanowire array (NWA) on an extended magnetic thin film in Fig. S2 by the coupled linearized Landau-Lifshitz-Maxwell equations [1]. h and w are the thickness and width of the nanowire; a is the periodicity; t denotes the thickness of the film. In the coordinate system in Fig. S2 $\hat{z} \parallel (\hat{x} \times \hat{y})$ is parallel to the nanowires. The magnetization \mathbf{M}_0 of the nanowires is always parallel to the \hat{z} -direction, while the saturated magnetization of the film $\tilde{\mathbf{M}}_0$ rotates in the film plane guided by the applied magnetic field. $\hat{\mathbf{z}}$ labels the direction of $\tilde{\mathbf{M}}_0$, $\hat{\mathbf{y}} \parallel (\hat{\mathbf{z}} \times \hat{\mathbf{x}})$, and θ is the angle between \mathbf{M}_0 and $\tilde{\mathbf{M}}_0$. We note that in our previous work [1], we have solved the collinear case with the magnetizations \mathbf{M}_0 and $\tilde{\mathbf{M}}_0$ being parallel to the

$\hat{\mathbf{z}}$ -direction. We extend here the collinear case with magnetizations \mathbf{M}_0 and $\tilde{\mathbf{M}}_0$ along the $\hat{\mathbf{z}}$ -direction [1] to non-collinear configurations.

We focus on the spectral region in which magnons are chiral, i.e. the vicinity of the NWA Kittel mode resonance.

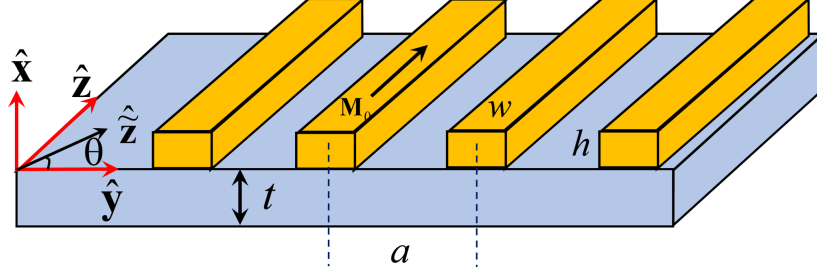


Fig. S2. Nanowire grating on the ferromagnetic film.

i. Ferromagnetic resonance of nanowire array

Under a uniform ac magnetic field, the macrospin (Kittel) modes in all wires precess in phase, forming a periodic potential with finite Fourier coefficients for momenta $k_y^n = n\pi/a$, where n are *positive even integers*. The transverse dynamic magnetization

$$\mathbf{M}_\alpha^K(\mathbf{r}) = \mathbf{m}_\alpha^K e^{-i\omega_K t} \Theta(h-x)\Theta(x) \sum_n 2f_n \cos(k_y^n y), \quad (\text{S1})$$

where $\alpha = (x, y)$; $f_n = (1 - \frac{1}{2}\delta_{n0}) \frac{2}{\pi n} \sin(\frac{w}{2}k_y^n)$, $\Theta(x)$ is the Heavyside step function.

$$\begin{aligned} \omega_K &= \mu_0 \gamma \sqrt{(H_{\text{app}}^z + M_0^z N_{xx})(H_{\text{app}}^z + M_0^z N_{yy})}, \\ \mathbf{m}_y^K &= i \sqrt{(H_{\text{app}}^z + M_0^z N_{xx}) / (H_{\text{app}}^z + M_0^z N_{yy})} \mathbf{m}_x^K, \end{aligned} \quad (\text{S2})$$

are the frequency and amplitude of a single-wire Kittel mode [2,3], where μ_0 and $-\gamma$ are the vacuum permeability and the gyromagnetic ratio of the electron spin, while $N_{\alpha\alpha}$ is a diagonal element of the demagnetization tensor [2-4]. We chose the normalization [5,6]

$$\int d\mathbf{r} [M_x^p(\mathbf{r}) \overline{M_y^p(\mathbf{r})} - \overline{M_x^p(\mathbf{r})} M_y^p(\mathbf{r})] = -i/2, \quad (\text{S3})$$

where the overbar indicates complex conjugation. For the mode Eq. (S1),

$$\mathbf{m}_x^K = \sqrt{\frac{a}{4hw} \sqrt{\frac{H_{\text{app}}^z + M_0^z N_{yy}}{H_{\text{app}}^z + M_0^z N_{xx}}}}, \quad \mathbf{m}_y^K = i \sqrt{\frac{a}{4hw} \sqrt{\frac{H_{\text{app}}^z + M_0^z N_{xx}}{H_{\text{app}}^z + M_0^z N_{yy}}}}. \quad (\text{S4})$$

ii. Spin waves in the YIG thin film

For compatibility with [1], we use here the coordinate system in Fig. S2, related to the $\hat{x} - \hat{y} - \hat{z}$ frame in the main text by a rotation of θ around the \hat{x} -axis. The Landau-Lifshitz equation reads [7]

$$\frac{d\tilde{\mathbf{M}}}{dt} = -\mu_0\gamma\tilde{\mathbf{M}} \times (\mathbf{H}_{\text{app}} + \tilde{\mathbf{H}}_d + \tilde{\mathbf{H}}_{\text{ex}}), \quad (\text{S5})$$

where the “tilde” labels the magnetization in the film, $\tilde{\mathbf{H}}_d$ represents the effective magnetic field due to the dipolar interaction [8]. The exchange field $\tilde{\mathbf{H}}_{\text{ex}} = \alpha_{\text{ex}}(\partial_x^2\tilde{\mathbf{M}} + \partial_y^2\tilde{\mathbf{M}} + \partial_z^2\tilde{\mathbf{M}})$ is parameterized by the exchange stiffness α_{ex} . We chose free boundary conditions [9-15] $d\tilde{\mathbf{M}}(x, \tilde{\mathbf{r}})/dx|_{x=0,-s} = 0$, where $\tilde{\mathbf{r}} = \tilde{y}\hat{\mathbf{y}} + \tilde{z}\hat{\mathbf{z}}$.

A spin wave $\tilde{\mathbf{M}}_{x,\tilde{y}}(x, \tilde{\mathbf{r}}) = \tilde{\mathbf{m}}_{x,\tilde{y}}^{\tilde{\mathbf{k}}}(x)e^{i\tilde{\mathbf{k}}\cdot\tilde{\mathbf{r}}}e^{-i\omega t}$ with $\tilde{\mathbf{k}} \equiv \tilde{k}_y\hat{\mathbf{y}} + \tilde{k}_z\hat{\mathbf{z}}$ can be expanded^{7,15} with $\tilde{\mathbf{m}}_{\pm}^{\tilde{\mathbf{k}}}(x) = \tilde{\mathbf{m}}_x^{\tilde{\mathbf{k}}}(x) \pm i\tilde{\mathbf{m}}_y^{\tilde{\mathbf{k}}}(x)$,

$$\tilde{\mathbf{m}}_{\pm}^{\tilde{\mathbf{k}}}(x) = \sum_{l=0}^{\infty} (\sqrt{2}/\sqrt{1+\delta_{l0}}) \cos(l\pi x/t) \tilde{\mathbf{m}}_{l,\pm}^{\tilde{\mathbf{k}}}. \quad (\text{S6})$$

The exchange energy for a perpendicular standing wave with index l is $\alpha_{\text{ex}}(l\pi/t)^2$. For $t \leq 20$ nm and spin waves with wavelength $2\pi/\tilde{k} \gtrsim 100$ nm, $\alpha_{\text{ex}}\tilde{k}^2 \ll \alpha_{\text{ex}}(l\pi/t)^2$ when $l \geq 1$, hence we retain only the lowest $l = 0$ mode [8,16]. Then

$$\omega_0 \begin{pmatrix} \tilde{\mathbf{m}}_{0,+}^{\tilde{\mathbf{k}}} \\ \tilde{\mathbf{m}}_{0,-}^{\tilde{\mathbf{k}}} \end{pmatrix} = \mu_0\gamma\tilde{M}_0 \begin{pmatrix} -\Omega_H - \alpha_{\text{ex}}\tilde{k}^2 - \frac{1}{2} + \frac{1}{2}\left(1 - \frac{\tilde{k}_y^2}{\tilde{k}^2}\right)f(\tilde{k}) & -\frac{1}{2} + \frac{1}{2}\left(1 + \frac{\tilde{k}_y^2}{\tilde{k}^2}\right)f(\tilde{k}) \\ \frac{1}{2} - \frac{1}{2}\left(1 + \frac{\tilde{k}_y^2}{\tilde{k}^2}\right)f(\tilde{k}) & \Omega_H + \alpha_{\text{ex}}\tilde{k}^2 + \frac{1}{2} - \frac{1}{2}\left(1 - \frac{\tilde{k}_y^2}{\tilde{k}^2}\right)f(\tilde{k}) \end{pmatrix} \begin{pmatrix} \tilde{\mathbf{m}}_{0,+}^{\tilde{\mathbf{k}}} \\ \tilde{\mathbf{m}}_{0,-}^{\tilde{\mathbf{k}}} \end{pmatrix} \quad (\text{S7})$$

with $\Omega_H \equiv H_{\text{app}}^z/\tilde{M}_0$ and $f(\tilde{k}) \equiv 1 - \frac{1}{|\tilde{k}_y|t} + \frac{1}{|\tilde{k}_y|t} \exp(-t|\tilde{k}_y|)$, and [8-11,17]

$$\omega_0 = \mu_0\gamma\tilde{M}_0 \sqrt{[(\Omega_H + \alpha_{\text{ex}}\tilde{k}^2 + 1 - f(\tilde{k}))][\Omega_H + \alpha_{\text{ex}}\tilde{k}^2 + \frac{\tilde{k}_y^2}{\tilde{k}^2}f(\tilde{k})]}. \quad (\text{S8})$$

For $\theta = 0$, we recover the Damon-Eshbach modes [20] with $\tilde{\mathbf{m}}_{0,\tilde{y}}^{\tilde{\mathbf{k}}} = i(B - 1)/(B + 1)\tilde{\mathbf{m}}_{0,x}^{\tilde{\mathbf{k}}}$ and

$$B = \frac{\frac{1}{2} - \frac{1}{2}\left(1 + \frac{\tilde{k}_y^2}{\tilde{k}^2}\right)f(\tilde{k})}{\frac{\omega_0}{\mu_0\gamma\tilde{M}_0} - \left(\Omega_H + \alpha_{\text{ex}}\tilde{k}_y^2 + \frac{1}{2}\right) + \frac{1}{2}\left(1 - \frac{\tilde{k}_y^2}{\tilde{k}^2}\right)f(\tilde{k})}. \quad (\text{S9})$$

With normalization Eq. (S3)

$$\tilde{\mathbf{m}}_{0,x}^{\tilde{\mathbf{k}}} = \sqrt{(B + 1)/[4t(B - 1)]}, \quad \tilde{\mathbf{m}}_{0,\tilde{y}}^{\tilde{\mathbf{k}}} = i\sqrt{(B - 1)/[4t(B + 1)]}. \quad (\text{S10})$$

At large momenta $\mu_0\gamma\tilde{M}_0(\Omega_H + \alpha_{ex}\tilde{k}^2 + 1/2)$ while the spin waves are circularly polarized $\tilde{\mathbf{m}}_{\tilde{y}}^{\tilde{k}} = i\tilde{\mathbf{m}}_{\tilde{x}}^{\tilde{k}} = i\sqrt{1/(4t)}$.

iii. Interlayer dipolar coupling

The interlayer dipolar coupling reads [7]

$$\hat{H}_d = -\mu_0\gamma^2 \frac{1}{4\pi} \int d\mathbf{r} \hat{\mathbf{S}}_\alpha(\mathbf{r}) \partial_\alpha \partial_\beta \int d\mathbf{r}' \frac{\hat{\tilde{\mathbf{S}}}_\beta(\mathbf{r}')}{|\mathbf{r}-\mathbf{r}'|}, \quad (\text{S11})$$

where $\hat{\mathbf{S}}_\alpha(\mathbf{r})$ and $\hat{\tilde{\mathbf{S}}}_\beta(\mathbf{r})$ are the transverse components of the spin operators in the NWA and the thin film with $\alpha = (x, y)$ and $\beta = (x, \tilde{y})$. In terms of the p 'th eigenmodes $\mathbf{M}_\alpha^p(\mathbf{r})$ and $\tilde{\mathbf{M}}_\beta^p(\mathbf{r})$ [4,18,19]:

$$\begin{cases} \hat{\mathbf{S}}_\alpha(\mathbf{r}, t) = \sqrt{2S} \sum_p [\mathbf{M}_\alpha^p(\mathbf{r}) \hat{\beta}_p(t) + \overline{\mathbf{M}_\alpha^p(\mathbf{r})} \hat{\beta}_p^\dagger(t)] \\ \hat{\tilde{\mathbf{S}}}_\beta(\mathbf{r}, t) = \sqrt{2\tilde{S}} \sum_p [\tilde{\mathbf{M}}_\beta^p(\mathbf{r}) \hat{\alpha}_p(t) + \overline{\tilde{\mathbf{M}}_\beta^p(\mathbf{r})} \hat{\alpha}_p^\dagger(t)] \end{cases}. \quad (\text{S12})$$

where $S = M_0/\gamma$, $\tilde{S} = \tilde{M}_0/\gamma$, while $\hat{\alpha}_p$ and $\hat{\beta}_p$ denote the magnon annihilation operators in the NWA and thin film, respectively. The interaction Hamiltonian between the lowest (perpendicular) spin wave mode in the film and Kittel mode in the NWA

$$\hat{H}_d = \sum_n (g_+^n \hat{\beta}_{+k_y^n} \hat{\alpha}_K^\dagger + g_-^n \hat{\beta}_{-k_y^n} \hat{\alpha}_K^\dagger + \rho_-^n \hat{\beta}_{-k_y^n} \hat{\alpha}_K + \rho_+^n \hat{\beta}_{+k_y^n} \hat{\alpha}_K + \text{h.c.}), \quad (\text{S13})$$

with

$$\begin{cases} g_+^n = -\mu_0\gamma\sigma_n\sqrt{\tilde{M}_0M_0} \int (\hat{\mathbf{m}}_{\text{YIG}}^+) \tilde{\mathbf{A}}^* (\hat{\mathbf{m}}_{\text{Co}}) e^{k_y^n x} dx, \\ g_-^n = -\mu_0\gamma\sigma_n\sqrt{\tilde{M}_0M_0} \int (\hat{\mathbf{m}}_{\text{YIG}}^-) \tilde{\mathbf{A}} (\hat{\mathbf{m}}_{\text{Co}}) e^{k_y^n x} dx, \\ \rho_-^n = -\mu_0\gamma\sigma_n\sqrt{\tilde{M}_0M_0} \int (\hat{\mathbf{m}}_{\text{YIG}}^-) \tilde{\mathbf{A}} (\hat{\mathbf{m}}_{\text{Co}}) e^{k_y^n x} dx, \\ \rho_+^n = -\mu_0\gamma\sigma_n\sqrt{\tilde{M}_0M_0} \int (\hat{\mathbf{m}}_{\text{YIG}}^+) \tilde{\mathbf{A}}^* (\hat{\mathbf{m}}_{\text{Co}}) e^{k_y^n x} dx. \end{cases} \quad (\text{S14})$$

Here, $\hat{\mathbf{m}}_{\text{YIG}}^\pm = (\tilde{m}_x^{\pm\tilde{k}_n}, \tilde{m}_y^{\pm\tilde{k}_n} \cos\theta)$, $\tilde{\mathbf{k}}_n = k_y^n (\cos\theta \hat{\mathbf{y}} + \sin\theta \hat{\mathbf{z}}) = k_y^n \hat{\mathbf{y}}$, $\hat{\mathbf{m}}_{\text{Co}} = (\hat{m}_x, \hat{m}_y)^T$, $\sigma_n = \frac{2}{n\pi} \sin\left(\frac{kw}{2}\right) (1 - e^{-kh})$ and $\tilde{\mathbf{A}} = \begin{pmatrix} 1 & i \\ i & -1 \end{pmatrix}$. We adopt the rotating wave approximation by disregarding ρ_-^n and ρ_+^n .

3. Angle-dependent spin wave spectroscopy

Fig. S3 displays the microwave transmission spectra S_{12} and S_{21} at 10 mT as a function of in-plane angle θ between the magnetizations of NWA and film, obtained by first saturating the magnetization with 200 mT. We focus on the $n = 20$ (dominantly)

exchange spin wave mode and rotate a 10 mT field from 180° degrees (AP configuration) to 360° or 0° (P configuration) with a step size of $\theta = 1^\circ$. We observe that the signal S_{12} in Fig. S3a is strongest for the P configuration, decreases with increasing angle and at $\sim 120^\circ$ vanishes in the noise. On the other hand, the S_{21} spectra a signal becomes visible at about 45° and is maximal for the AP configuration.

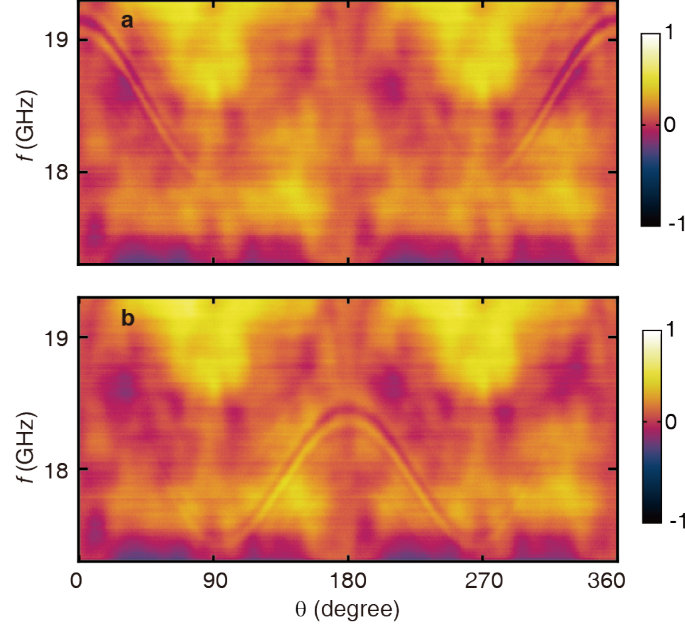


Fig. S3. Angle dependent spin wave spectroscopy. Transmission spectra (a) S_{12} and (b) S_{21} of spin wave mode $n=20$ at 10 mT.

4. Control measurements with Al_2O_3 spacer

Fig. S4 shows control measurements on a sample with 2 nm thick Al_2O_3 between the NWA and the YIG film, keeping other fabrication parameters as in Fig. 1, thereby eliminating exchange coupling between the YIG film and Co nanowires. The unidirectional excitation of ESWs with mode number $n=20$ in fig. S4a and b is clearly visible but weaker than in Fig. 1 of the main text as expected from the larger separation between YIG film and Co NWA.

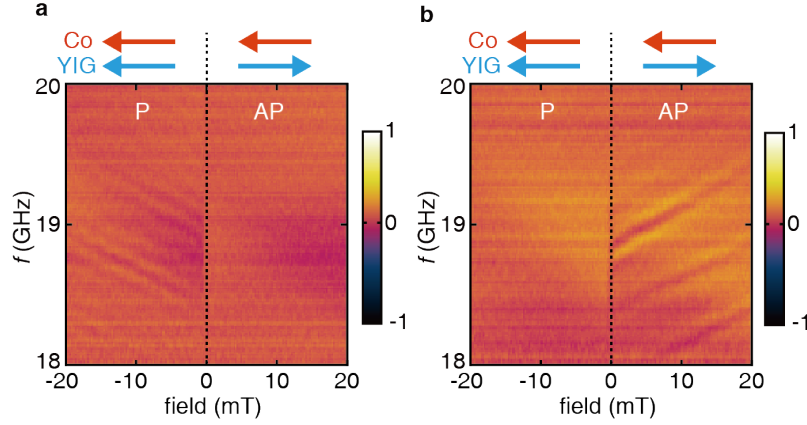


Fig. S4. Transmission spectra of a sample with Al_2O_3 spacer. **a**, Spin wave transmission spectra S_{21} for exchange spin waves. The mode number $n=20$ is presented which corresponding to the spin wave wavelength $\lambda \sim 60$ nm. **b**, Spin wave transmission spectra S_{12} in the same region of the spectra.

5. Micromagnetic simulations of the Co/YIG hybrid nanostructure

In order to validate the analytic model we also simulated the spectra using the public object-oriented micromagnetic framework (OOMMF, <http://math.nist.gov/oommf>). We simulate a YIG film with dimensions $15 \mu\text{m} \times 5 \mu\text{m} \times 20 \text{ nm}$ (yzx) and 15 equally 600 nm spaced Co nanowires with dimensions $110 \text{ nm} \times 5 \mu\text{m} \times 20 \text{ nm}$ (yzx) along the y axis. The saturation magnetizations M_s are 1430 kA m^{-1} and 140 kA m^{-1} and the exchange stiffnesses α_{ex} are chosen as $13 \times 10^{-12} \text{ J m}^{-1}$ and $3 \times 10^{-12} \text{ J m}^{-1}$ for Co and YIG, respectively, and disregard interfacial exchange. The Gilbert damping parameters α are 8×10^{-5} for YIG and 0.01 for Co. We solve the Landau-Lifshitz equations on a mesh with dimensions $5 \text{ nm} \times 500 \text{ nm} \times 20 \text{ nm}$ (yzx). We first establish the equilibrium state with a static magnetic field in the z direction. We then apply a homogenous ac magnetic field pulse in the y direction of the form $H_{\text{ex}} = 0.2 \text{ mT} \sin(2\pi \times 100 \text{ GHz} (t - 100 \text{ ps})) / (2\pi \times 100 \text{ GHz} (t - 100 \text{ ps}))$ [Ki-Suk Lee, Dong-Soo Han, and Sang-Koog Kim, PRL 102, 127202 (2009)]. The step size of the time-dependent simulation is 20 ps over 4 ns and a fast Fourier transform of the magnetization dynamics leads to the spectra in Figure S5. The Co nanowires are observed to switch at 80 mT from the AP to the P state. The resonance mode of the Co nanowires anti-crosses with high-momentum exchange spin waves with mode numbers $n = 18$ and $n = 20$ with coupling strengths plotted in Fig. 4c of the main text.

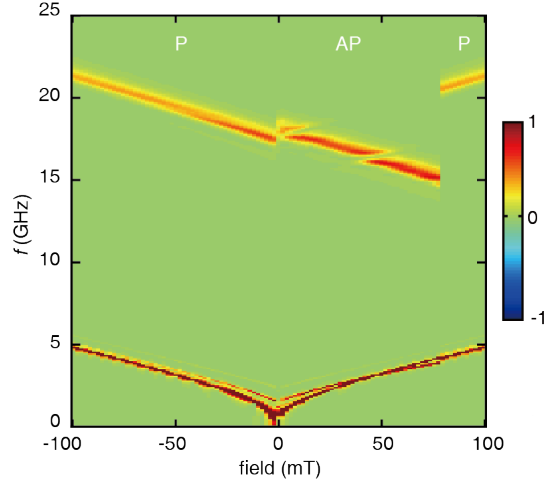


Fig. S5. Reflection spectra S_{11} from micromagnetic simulations. The external magnetic field (abscissa) is applied in-plane and parallel to the nanowires. We first saturate the magnetizations at -200 mT and then sweep the field from -100 mT to 100 mT. The lower branch in the spectra is the YIG resonance while the upper branch is that of the Co nanowires. The anti-crossings between the Co resonance mode and the YIG exchange spin waves for positive fields is a measure of their coupling.

6. Angle-dependent reflection spectra

Fig. S6 shows the reflection spectra S_{11} as a function of the direction of an applied field with fixed strength 60 mT. The latter is first applied perpendicular to the nanowires ($\theta = 90^\circ$) and then swept to 270° . The gap observed when the Kittel resonance of the Co nanowires anti-crosses with the exchange spin wave with mode number $n=16$ persists over a large interval from 130° to 230° .

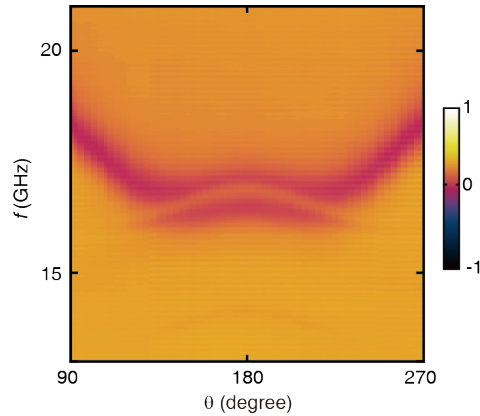


Fig. S6. Angle dependent spin wave reflection spectrum S_{11} . An in-plane magnetic field of 60 mT is first applied normal to the nanowires and then rotated from 90° to 270° . The angle step is 3° .

7. Transmission spectra of the $n=16$ and $n=18$ exchange spin waves

Figure S7 shows the transmission spectra of YIG spin waves with mode numbers $n=16$

and $n=18$. An external magnetic field is applied first at -300 mT and then swept from -20 mT to 20 mT. The propagation is unidirectional for both $n=16$ and $n=18$. In the P (AP) configuration, the spin wave signal only exists in S_{21} (S_{12}) spectra, in agreement with the chirality of the $n=20$ mode shown in Fig. 1 in the main text.

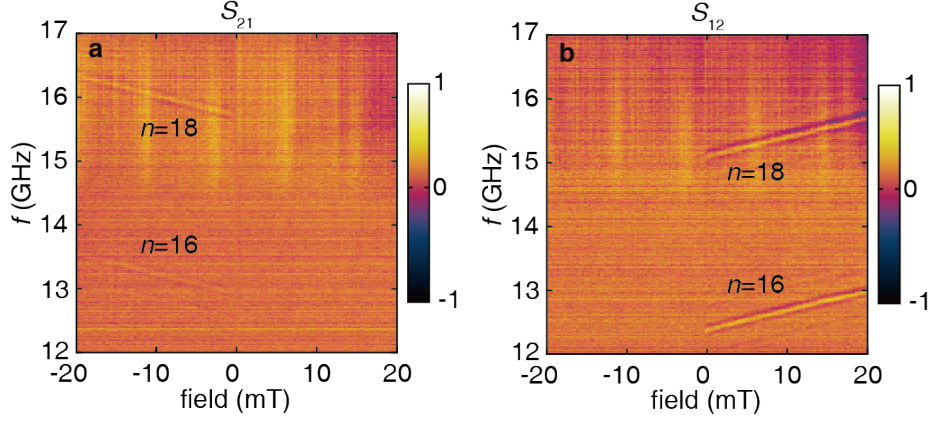


Fig. S7. Transmission spectra of ESWs with mode number $n=16$ and $n=18$. The external magnetic field is first applied at -300 mT and then swept from -20 mT to 20 mT. The field step is 0.25 mT.

8. Extraction of spin wave resonance frequencies and excitation efficiencies

Fig. S8(a) illustrated the assignment of the resonance frequencies from the transmission spectra of the $n=20$ mode. The signals launched by CPW1 cause an interference at CPW2 by the phase difference accumulated during transmission. We simply chose the maximum of the spin wave signal as the average spin wave resonance frequency. The spin wave signal strengths of different spin wave modes at fixed magnetic field of 2 mT are shown in Fig. S8b after normalizing to the $n=2$ mode. The $n=10$ and $n=12$ modes are missing because the signal strength is below the noise level. The $n=20$ mode is the strongest since close to resonant with the Co nanowire at this magnetic field.

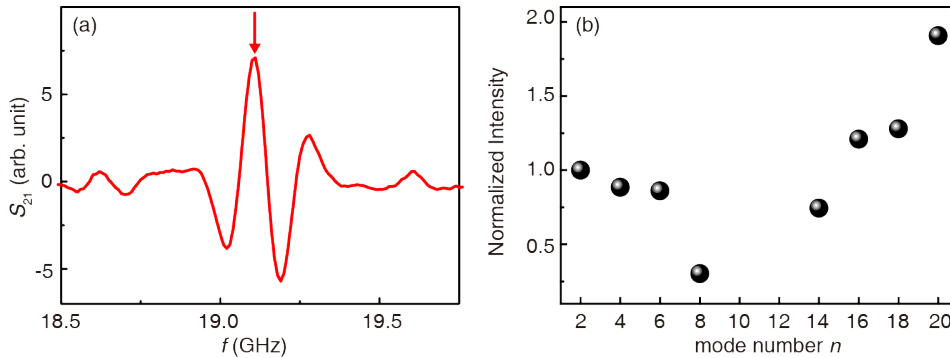


Fig. S8. Extraction of spin wave resonance frequencies and the spin wave excitation efficiency. a, The single lineplot of the transmission spectra S_{21} at -10 mT. The imaginary part extracted from the VNA

of $n=20$ iSSW is shown as an example. The arrow shows the resonance peak of the spin waves where we read. b, Spin-wave excitation efficiency as a function of the mode number n extracted from S_{12} spectra at 2 mT. The efficiency is normalized taking the value for $n = 2$ as 1.0.

9. Nonreciprocity of dipole-exchange spin waves [13,21]

We model the chirality due to the surface-exchange-mediated excitation, which is governed by the ellipticity of the magnetic precession. The results are plotted as open triangles in Fig. 2 (e) and (f). Since we have to go to large wave numbers spin waves, the Damon-Eshbach theory [20] is not sufficient, rather the dipole-exchange spin wave modes must be considered [13,21].

The LLG equation with exchange interaction

$$i\omega m_y = -\omega_M h_z + (\omega_H - \alpha_{\text{ex}} \nabla^2) m_z, \quad (\text{S15})$$

$$i\omega m_z = \omega_M h_y - (\omega_H - \alpha_{\text{ex}} \nabla^2) m_y. \quad (\text{S16})$$

can be rewritten as

$$m_y = \frac{1}{(\omega_H - \alpha_{\text{ex}} \nabla^2)^2 - \omega^2} [(\omega_H - \alpha_{\text{ex}} \nabla^2) \omega_M h_y - i\omega \omega_M h_z], \quad (\text{S17})$$

$$m_z = \frac{1}{(\omega_H - \alpha_{\text{ex}} \nabla^2)^2 - \omega^2} [(\omega_H - \alpha_{\text{ex}} \nabla^2) \omega_M h_z + i\omega \omega_M h_y]. \quad (\text{S18})$$

Here, $\omega_H = \gamma H_0$, $\omega_M = \gamma M_0$ and α_{ex} is the stiffness constant. The dipolar field $\mathbf{h} = \nabla \psi$ satisfies $\nabla \cdot (\mathbf{h} + \mathbf{m}) = 0$, which leads to

$$0 \equiv [(\omega_H - \alpha_{\text{ex}} \nabla^2)^2 - \omega^2] \nabla \cdot (\mathbf{h} + \mathbf{m}), \quad (\text{S19})$$

$$= \{[(\omega_H - \alpha_{\text{ex}} \nabla^2)^2 - \omega^2 + (\omega_H - \alpha_{\text{ex}} \nabla^2) \omega_M] \nabla^2 - (\omega_H - \alpha_{\text{ex}} \nabla^2) \omega_M \partial_x^2\} \psi. \quad (\text{S20})$$

In Fourier space

$$[(\omega_H + \alpha_{\text{ex}} k^2 + \alpha_{\text{ex}} k_z^2)^2 - \omega^2 + (\omega_H + \alpha_{\text{ex}} k^2 + \alpha_{\text{ex}} k_z^2) \omega_M] (k^2 + k_z^2) - (\omega_H + \alpha_{\text{ex}} k^2 + D k_z^2) \omega_M k^2 \cos^2 \theta = 0. \quad (\text{S21})$$

For $\theta = \pi/2$, Eq. (S21) reduces to

$$[(\alpha_{\text{ex}} k_z^2)^2 + \alpha_{\text{ex}} k_z^2 (\omega_M + 2\tilde{\omega}_H) + \tilde{\omega}_H^2 + \tilde{\omega}_H \omega_M - \omega^2] (k^2 + k_z^2) = 0, \quad (\text{S22})$$

where $\tilde{\omega}_H = \omega_H + \alpha_{\text{ex}} k^2$ with k being the in-plane wave vector. For a frequency ω , there are six solutions of k_z ,

$$k_z^2 = -k^2, \frac{-(2\tilde{\omega}_H + \omega_M) - \sqrt{\omega_M^2 + 4\omega^2}}{2\alpha_{\text{ex}}}, \frac{-(2\tilde{\omega}_H + \omega_M) + \sqrt{\omega_M^2 + 4\omega^2}}{2\alpha_{\text{ex}}}. \quad (\text{S23})$$

The coefficients a_j of the expansion

$$\psi = \sum_{j=1}^6 a_j e^{ik_z^j z} e^{ik_x x} e^{ik_y y} \quad (\text{S24})$$

are determined by the boundary condition at the film interfaces [3]

$$\psi|_{z>s/2} = ce^{-k_z^e z} e^{ik_x x} e^{ik_y y}, \quad (\text{S25})$$

$$\psi|_{z<0} = de^{k_z^e z} e^{ik_x x} e^{ik_y y}. \quad (\text{S26})$$

In particular,

$$h_y|_{\pm s/2}^{\text{in}} = h_y|_{\pm s/2}^{\text{out}} \quad (\text{S27})$$

$$h_z + m_z|_{\pm s/2}^{\text{in}} = h_z|_{\pm s/2}^{\text{out}} \quad (\text{S28})$$

as well as the Rado-Weertman exchange boundary condition [22]

$$\mathbf{M} \times [\nabla_{\mathbf{M}} E_{\text{an}} - 2\alpha_{\text{ex}} \partial_n \mathbf{M}]|_{\pm s/2} = 0, \quad (\text{S29})$$

where ∂_n is the partial derivative along the outward normal direction to the surface.

When the surface anisotropy E_{an} vanishes, the exchange boundary conditions reduce to the “free” ones:

$$\partial_z m_y|_{\pm s/2} = 0, \quad (\text{S30})$$

$$\partial_z m_z|_{\pm s/2} = 0. \quad (\text{S31})$$

Substituting Equations (S24)-(S26) into these free boundary conditions (S30-S31) [14]

$$\sum_j [ik_z^j(1 + \kappa_j) - k_y v_j + k_z^e] e^{ik_z^j s/2} a_j = 0 \quad (\text{S32})$$

$$\sum_j [ik_z^j(1 + \kappa_j) - k_y v_j - k_z^e] e^{-ik_z^j s/2} a_j = 0 \quad (\text{S33})$$

$$\sum_j [\kappa_j k_y k_z^j - i v_j k_z^{j2}] e^{ik_z^j s/2} a_j = 0 \quad (\text{S34})$$

$$\sum_j [\kappa_j k_y k_z^j - i v_j k_z^{j2}] e^{-ik_z^j s/2} a_j = 0 \quad (\text{S35})$$

$$\sum_j [\kappa_j k_z^{j2} + i v_j k_y k_z^j] e^{ik_z^j s/2} a_j = 0 \quad (\text{S36})$$

$$\sum_j [\kappa_j k_z^{j2} + i v_j k_y k_z^j] e^{-ik_z^j s/2} a_j = 0 \quad (\text{S37})$$

from which the dipole-exchange spin wave dispersion as well as the spatial profile of the spin wave mode amplitudes can be calculated. In Eqs. (S32)-(S37), we use the short hand

$$\kappa_j = \frac{(\tilde{\omega}_H + \alpha_{\text{ex}} k_z^{j2}) \omega_M}{(\tilde{\omega}_H + \alpha_{\text{ex}} k_z^{j2})^2 - \omega^2}, \quad (\text{S38})$$

$$v_j = \frac{\omega \omega_M}{(\tilde{\omega}_H + \alpha_{\text{ex}} k_z^{j2})^2 - \omega^2}. \quad (\text{S39})$$

The difference between the local amplitudes of \mathbf{m}_k and \mathbf{m}_{-k} at the interface with the nanowires leads to the chirality of the surface-exchange-mediated excitations. Since both excitation and detection efficiencies are proportional to $|\mathbf{m}|^2$ at the interface, the efficiency of chirality generation (Eq. (2) in the main text) by $|\mathbf{m}|^4$ at the detector

$$\eta_{\text{ex}} = \frac{|\mathbf{m}_k(\frac{S}{2})|^4 - |\mathbf{m}_{-k}(\frac{S}{2})|^4}{|\mathbf{m}_k(\frac{S}{2})|^4 + |\mathbf{m}_{-k}(\frac{S}{2})|^4}. \quad (\text{S40})$$

The calculated η_{ex} in Figures 2(e,f) of the main text as a function of wavenumber do not depend on the relative orientation of the Co nanowires since we consider excitation/detection by the CPWs.

10. Sample fabrications and measurement techniques

The 20-nm-thick YIG thin film is deposited on a 0.5-mm-thick (111) oriented gadolinium gallium garnet (GGG) substrate by the sputtering deposition. The deposition is at room temperature first and the annealing is in O₂ at 800 °C. A YIG

waveguide with the dimensions of $250\ \mu\text{m} \times 90\ \mu\text{m}$ is fabricated by the photolithography and the ion beam etching. Tapering the YIG waveguide at both ends prevents spin wave interference by reflection. The array of Co nanowires is patterned on top of the YIG waveguide by a lift-off process using electron beam lithography and electron beam evaporation. The width and the period of the Co nanowires are 110 nm and 600 nm respectively. A pair of identical gold coplanar waveguides (CPW) are then patterned on top of the Co nanowires with signal line and ground line widths of $2\ \mu\text{m}$. The gap between the signal line and the ground line is $1.6\ \mu\text{m}$. The center-to-center distance between the two CPWs is $15\ \mu\text{m}$.

The spin-wave measurement is conducted by a vector network analyzer(VNA)-based all electrical technique. The Rohde & Schwarz ZVA 40 VNA used in the experiment offers a frequency range from 10 MHz to 40 GHz. The CPWs are connected via the GGB MODEL 40A microwave probes. The power used in the experiments is 0 dBm. During the measurement, the VNA sends a microwave current to the CPW and generates an alternating magnetic field that excites the spin waves in the ferromagnetic film. The VNA also picks up spin wave-induced magnetic flux changes such that S -parameters with both reflection (S_{11} and S_{22}) and transmission (S_{12} and S_{21}) spectra can be extracted.

The μ -BLS measurements were carried out by a diffraction limited laser beam with a diameter of about 235 nm on both sides of the CPW antennas. The backscattered light is analysed in frequency by a (3+3)-tandem Sandercock-type Fabry-Pérot interferometer. Here RF picoprobes connected to a microwave generator working up to 20 GHz and with +20 dBm power excited the spin waves. Sample stabilization against mechanical drifts was achieved by the TFPDAS4 software, which employs both an image recognition and an auto-focusing routine to compensate, in real time, for drifts of the sample position and of the focus distance.

References

- [1] T. Yu, C. Liu, H. Yu, Y. M. Blanter and G. E. W. Bauer, *Phys. Rev. B* **99**, 134424 (2019).
- [2] J. Ding, M. Kostylev & A. O. Adeyeye, *Phys. Rev. B* **84**, 054425 (2011).
- [3] C. Kittel, *Quantum Theory of Solids* (Wiley, New York, 1963).
- [4] C. Kittel, *Phys. Rev.* **73**, 155 (1948).

-
- [5] R. Verba, G. Melkov, V. Tiberkevich & A. Slavin, *Phys. Rev. B* **85**, 014427 (2012).
- [6] L. R. Walker, *Phys. Rev.* **105**, 390 (1957).
- [7] L. D. Landau and E. M. Lifshitz, *Electrodynamics of Continuous Media*, 2nd ed. (Butterworth-Heinenann, Oxford, 1984).
- [8] B. A. Kalinikos, *Sov. J. Phys.* **24**, 718 (1981).
- [9] K. Yu. Guslienko, S. O. Demokritov, B. Hillebrands, and A. N. Slavin, *Phys. Rev. B* **66**, 132402 (2002).
- [10] V. Vlaminck and M. Bailleul, *Phys. Rev. B* **81**, 014425 (2010).
- [11] F. Zighem, Y. Roussigne, S.-M. Cherif, and P. Moch, *J. Phys.: Condens. Matter* **19**, 176220 (2007).
- [12] R. E. De Wames and T. Wolfram, *Appl. Phys. Lett.* **15**, 297 (1969).
- [13] T. Wolfram and R. E. De Wames, *Phys. Rev. Lett.* **24**, 1489 (1970).
- [14] R. L. Stamps and B. Hillebrands, *Phys. Rev. B* **44**, 12417 (1991).
- [15] R. L. Stamps, *Phys. Rev. B* **49**, 339 (1994).
- [16] M. Kostylev, *J. Appl. Phys.* **113**, 053907 (2013).
- [17] M. J. Hurben and C. E. Patton, *J. Magn. Magn. Mater.* **139**, 263 (1995).
- [18] A. Kamra and W. Belzig, *Phys. Rev. Lett.* **116**, 146601 (2016).
- [19] T. Holstein and H. Primakoff, *Phys. Rev.* **58**, 1098 (1940).
- [20] R. W. Damon and J. R. Eshbach, *J. Phys. Chem, Solids* **19**, 308 (1961).
- [21] B. A. Kalinikos, M. P. Kostylev, N. V. Kozhus, and A. N. Slavin, *J. Phys.: Condens. Matter* **2**, 9861 (1990).
- [22] G. T. Rado and J. R. Weertman, *J. Phys. Chem. Solids* **11**, 315 (1959).